Research Article Vol. 34, No. 3 / 9 Feb 2026 / Optics Express 3691

Optics EXPRESS

Focus and depth of field tunable detection system for compact quantum sensors

KAI FRYE-ARNDT,[1,2,*] ARNE WACKER,[2] PATRICK BRUNSSEN,[3] TIL DRALLE,[1] HOLGER AHLERS,[2] WALDEMAR HERR,[2] ERNST RASEL,[1] AND CHRISTIAN SCHUBERT[2]

[1] *Leibniz University Hannover, Institute for Quantum Optics, 30167 Hannover, Germany*
[2] *German Aerospace Center (DLR), Institute for Satellite Geodesy and Inertial Sensing, 30167 Hannover, Germany*
[3] *German Aerospace Center (DLR), Institute for Satellite Geodesy and Inertial Sensing, Am Fallturm 9, 28359 Bremen, Germany*
[*] *frye@iqo.uni-hannover.de*

Abstract: Absorption imaging is a well-established method for determining both the atom number and spatial distribution of atomic ensembles, traditionally limited to a single focal plane and a fixed depth of field. However, as atom optics experiments grow more complex, atomic clouds can exceed the depth of field or leave the focal plane, as seen in large atomic arrays or bubble Bose-Einstein condensates (BECs). Here, we present an absorption imaging system that allows for tuning the object distance of 88.9 mm by ±5 mm and the depth of field from 26 µm to 203 µm. We determine performance metrics relevant for atomic experiments, such as the resolution and the optical distortion.

1. Introduction

Absorption imaging relies on the attenuation of light beams passing through atomic clouds [1,2]. As atoms absorb photons from the imaging beam, they become excited and emit photons via spontaneous emission in random direction, thus locally reducing the intensity of the imaging beam and casting a shadow that forms an image. By comparing the beam containing the shadow of the atoms to a reference beam without atoms, the column density of the atomic cloud can be extracted. A typical absorption imaging setup consists of a camera, an aperture stop, and a set of solid lenses, arranged to have the atoms at an object distance s_O and create an image onto the camera sensor at distance s_I [3–7]. However, such a setup lacks flexibility, as the focal length and the depth of field (DOF) are fixed after assembly.

In this work, we present an imaging system for detecting ultracold atoms, where the initial object distance $s_O = 88.9$ mm can be tuned by ±5 mm. This tunability is achieved by using a focus tunable liquid lens (ML-20-37 from *Optotune*), which changes the effective focal length (EFL). The EFL is the overall focal length of the imaging system and by changing it, the s_O can be adjusted even when the atom-facing lens and the camera distance s_I are fixed, such that the lens equation $1/\mathrm{EFL} = 1/s_O + 1/s_I$ holds. Liquid lenses have been used previously to transport cold atoms [8] and for microscopy [9,10], as well as 3D reconstruction of atomic arrays [11], but with a tunable range of only 100 µm. Our system advances these techniques by extending the tunable range by two orders of magnitude while maintaining a compact design suitable for mobile quantum sensors [12,13]. Furthermore, the DOF can be varied from 26 µm to 203 µm by using a custom-built adjustable iris aperture.

The tunable EFL could, in principle, be realized by mechanically translating optical components. However, using liquid lenses enables a design with minimal moving parts, greatly improving

#582238 https://doi.org/10.1364/OE.582238
Journal © 2026 Received 22 Oct 2025; revised 12 Dec 2025; accepted 11 Jan 2026; published 26 Jan 2026

robustness against vibrations and shocks. Other tuning approaches, such as Moiré lenses [14] or liquid-crystal spatial light modulators [15], are strongly wavelength dependent, complicating simultaneous imaging of rubidium and potassium. In contrast, deformable mirrors [16] are wavelength independent, but their control systems are more bulky, which complicates accommodation to setups with stringent size, weight, and power constraints.

A tunable detection system offers several advantages over a static system. First, it allows for imaging atoms at different axial distances from the imaging system. This is beneficial for experiments where atoms are transported during the experiment, the ensembles are in free fall along the line of sight or multiple spatially separated atomic clouds are present [17]. The latter includes mirrored images of clouds when the imaging beam is reflected at an angle to a surface close to the atoms like in experiments using atom chip technology [5,7]. The tunable DOF enables sharp imaging of multiple clouds simultaneously, while the adjustable EFL allows focusing on specific clouds. Second, utilizing tunable lenses enhances flexibility in engineering the imaging system, especially when lenses with certain focal lengths are not available or rapid iterations in the design process are required. Third, tuning the EFL opens up possibilities for advanced imaging techniques, such as multi-camera off-resonance defocus imaging [6], but with a single camera. For instance, the atomic cloud can be reconstructed by capturing multiple images at different focal length settings, allowing for partially non-destructive imaging with increased sensitivity. Finally, tunable detection systems aid in investigating hollow bubble Bose-Einstein condensates (BECs) [18,19], where the curved surface is a challenging object to image with a small depth of field and a fixed focal plane, especially as the bubble BEC expands. The shells typically have a thickness of only a few microns [20], allowing a single slab of the bubble to lie within the smallest DOF achieved here. Although the full bubble can extend to millimeter scales, exceeding our maximum DOF, the increased DOF remains advantageous for studying the curved surface, as different surface elements can be brought into focus.

The paper is organized as follows. First the optical system design for a compact apparatus suited for space-borne experiments is presented (section 2) which we characterize in the following sections. We determine the resolution via the modulation transfer function (MTF) obtained from images of a star target (section 3). We extent the method of determining the MTF by performing scans through the focal plane to obtain the through-focus MTF. This through-focus MTF is used to determine the DOF (section 4) for different settings of the iris aperture. In section 5 we quantify the optical distortion that our imaging system exhibit. Section 6 shows the tuning range of the object distance and the change in magnification. Finally, we conclude our results in section 7.

2. Design and description of the imaging system

The mechanical setup is tailored to meet the demands of an ultracold atom experiment planned for launch to the International Space Station [21]. The imaging system is optimized for a wavelength range of 767 nm to 780 nm, ensuring compatibility with all natural isotopes of rubidium and potassium. To minimize redundancy, all measurements were conducted at 780 nm. The first elements to consider are the lenses L1 and L2 in Fig. 1(a), which already realize a functional imaging system. L1 determines the front focal length f_{front} and L2 the back focal length f_{back}, where the camera (GS3-U3-89S6M-C from *Teledyne FLIR*) has to be placed to obtain optimal results. Because the front and back focal lengths generally differ, the system exhibits a magnification of approximately $m \approx f_{\mathrm{back}}/f_{\mathrm{front}}$, which becomes exact in the thin lens limit. We have chosen a combination of two lens doublets. L1 is the lens 49-795 (f = 88.9 mm) and L2 is 49-362 (f = 150 mm) from *Edmund Optics*. To these lenses we add the iris, the tunable lens (TL) and a mirror. The iris is placed close to the static lenses L1 and L2 for maximum effect in aperture change. The TL is positioned between the static lens system and the camera. The closer the TL is to the static lens system, the larger a change in the focal length f_{TL} of the TL effects the EFL.

However, the TL is expected to introduce aberrations and distortions compared to an optimized aspherical lens. These unwanted effects are minimized by placing the TL closer to the camera thus reducing its effect on the imaging system. The requirements on tunability and imaging quality determine the optimal position of the TL. To showcase the extended design freedom offered by freely choosing the focal length within the available range, we tune the TL to achieve a shorter path between the mirror and camera. Without the TL, this would require replacing lens L2. We use *Ansys Zemax OpticStudio* to optimize the system configuration, ensuring a tunable range slightly exceeding $\Delta s_O = \pm 5$ mm. Finally, in between the static lenses and the camera, we place a mirror to fold the setup. This suits compact apparatuses and makes the setup more robust, since it shortens the lever arm. Additionally, the option of redirecting the beam path enables a horizontal placement of the TL to minimize coma due to the gravitational sag of the liquid without restriction to a single detection axis. The lens and the iris are actuated with non-magnetic piezoelectric motors (ANR101-03674 from *Attocube*), which are spatially separated from the tunable lens. This approach reduces thermal drifts and spurious magnetic fields compared to components with integrated drive electronics. A photo of the realized setup is shown in Fig. 1(c).

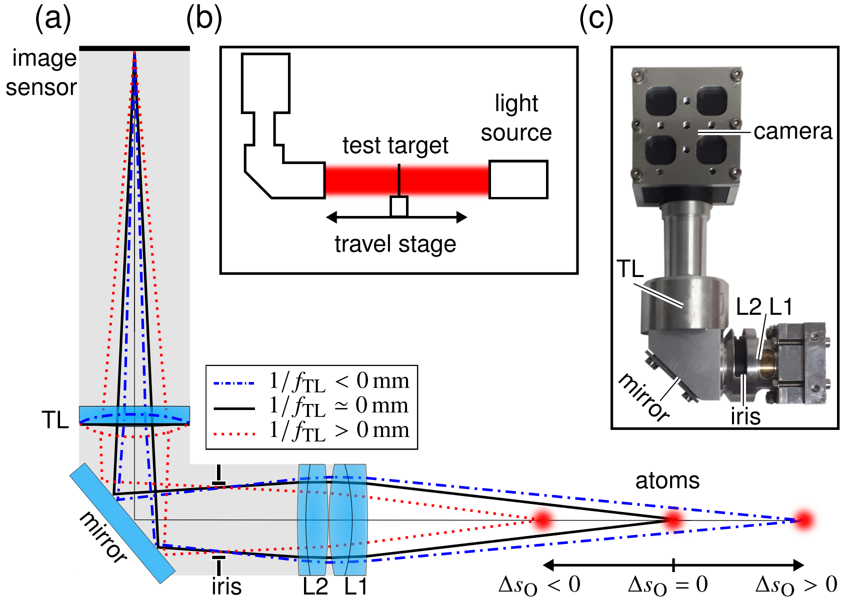

Fig. 1. Realization of the tunable detection system. (a) Schematic of the imaging system. The static lenses L1 and L2 are closest to the atoms (red clouds), followed by a motorized iris. A mirror folds the light propagation path. The tunable lens (TL), which adjusts the effective focal length (EFL), is placed between the mirror and the camera sensor. For a fixed image distance, the change in EFL shifts the object distance s_O by Δs_O, with Δs_O corresponding to the TL having zero curvature. Blue dash-dotted lines, thick black lines and red dotted lines show the beam paths for different TL settings. Closing the iris will not change the EFL, but decreases the angle of the cone of light that can enter the imaging system, therefore decreasing the depth of field (DOF). (b) Measurement setup. An optical test target is moved by a travel stage through the focal plane. The light source is either a collimated laser beam or a filament lamp. (c) Photo of the detection system. The positions of the optical elements are labeled, but not directly visible due to the enclosure.

3. Determination of the resolution via the MTF

The resolution of an imaging system is the ability to resolve and distinguish structures and objects. The resolution is characterized by the modulation transfer function (MTF), which specifies how the amplitudes of different spatial frequencies relate to the captured amplitudes in the image plane. The MTF is determined by taking images of an optical test target placed in the focal plane of the imaging system (Fig. 1(b)), in our case, a star target (R1L1S3P by *Thorlabs*), shown in Fig. 2(a). We set the iris to maximum free aperture and the TL to the central focal length $\Delta f = 0$. The analysis of the pictures is as follows: First, the center of the star target is determined by the intersection of the spokes using a probabilistic Hough line algorithm [22]. Second, using the center of the star target, the image is transformed into polar coordinates (Fig. 2(b)). Third, for each radius the pixel values are used to determine the Michelson contrast [23]

$$C = \frac{\overline{I_{\mathrm{max}}} - \overline{I_{\mathrm{min}}}}{\overline{I_{\mathrm{max}}} + \overline{I_{\mathrm{min}}}}, \tag{1}$$

where $\overline{I_{\mathrm{max}}}$ ($\overline{I_{\mathrm{min}}}$) is the average pixel value of the maxima (minima) (Fig. 2(c)). Finally, the contrast C is plotted against the spatial frequency in units of line pairs per millimeter (Fig. 2(d)). Here, the apparent spatial frequency determined by the pixel size of the camera sensor needs to be multiplied by the magnification m to get the object-space MTF. The magnification is determined by the apparent size of the center circle of the star target divided by the known size of the center circle.

Experiments with atomic clouds typically use monochromatic, coherent light to address specific atomic states. However, key imaging-system characteristics, such as resolution, depth of field, and distortion, are either intrinsic to the optics and do not depend on whether the illumination is coherent or incoherent, or can be easily transformed into each other. Practically, both coherent and incoherent illumination offer distinct advantages and limitations. Coherent illumination reveals clipping, internal reflections, and unwanted apertures through diffraction rings, but also produces interference patterns that make the characterization apparatus sensitive to small misalignments and tilts of the light source and target relative to the imaging system under test. These artifacts originate from the characterization setup and degrade the measured MTF, rather than reflecting properties of the imaging system itself. Incoherent light avoids interference and is therefore less affected by such alignment errors, motivating its use in most of our measurements.

For the determination of the MTF, we illuminate the target with both coherent and incoherent light. As a coherent light source we use a temperature stabilized external cavity diode laser. A filament lamp provides incoherent illumination, which we spectrally filter using a Schott UG-1 glass to match the design wavelength range. Because the lamp emits non-uniformly we homogenize the illumination using a method analogous to bokeh generation in photography [24]. A lens (LB1761-B-ML, Thorlabs) images the filament from a distance larger than its focal length, and an iris placed between them is closed to truncate the beam until uniform illumination is obtained.

Figure 2(d) shows different MTFs for the imaging system. The orange dotted line shows the calculated diffraction limit for an aperture diameter of 22.4 mm, resulting in a spatial cut-off frequency of $\mathrm{f}_{\mathrm{cut,diff}} = 250$ 1p/mm. The simulated MTF for the imaging system (blue line) follows the diffraction limit, even reaching the same cut-off spatial frequency. The green line shows the measurement results obtained with incoherent illumination. It closely follows the diffraction limit and the curve calculated with Zemax until a spatial cut-off frequency $\mathrm{f}_{\mathrm{cut,star}} = 115$ 1p/mm of the star target. The measured MTF is above the simulated MTF for frequency 50 lp/mm to 100 lp/mm, which hints at apodization being present in the imaging system [25,26]. Beyond $\mathrm{f}_{\mathrm{cut,star}}$ the contrast drops to <0.03, which is caused by intensity noise.

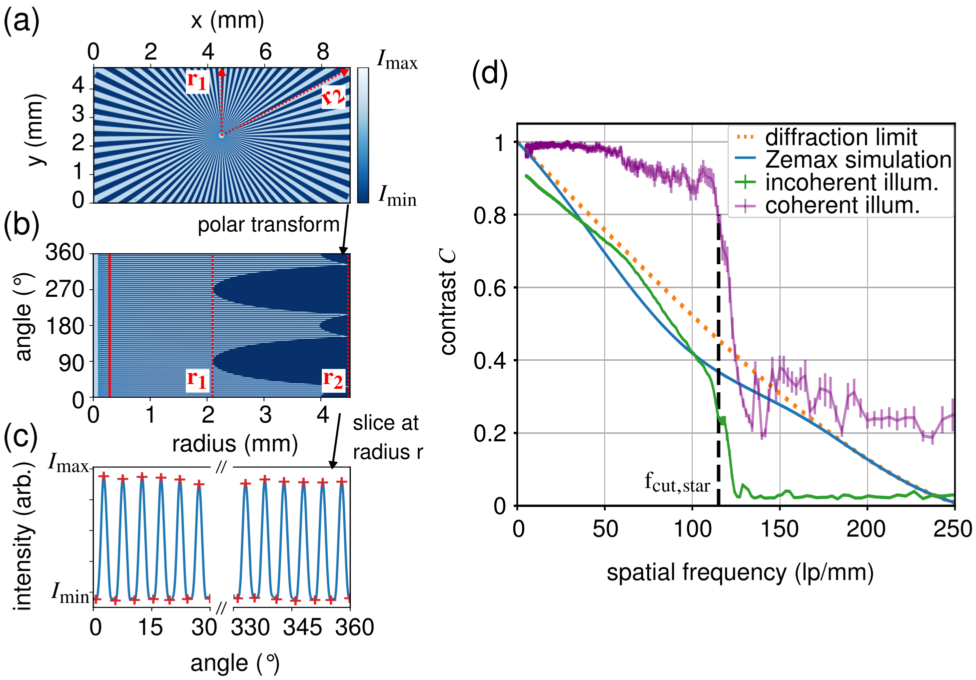

Fig. 2. Determination of the MTF of the imaging system. (a) An image of the star target. The length scales are in object space, therefore showing the field of view. (b) The picture of the star target is transformed into polar coordinates. For illustration purposes we set the intensity value to $I_{\min}$ for radii exceeding the rectangular format. The red line gives an example slice along a constant radius, which corresponds to a spatial frequency. (c) The intensities along the red slice are shown. The average value of the maxima and minima gives the contrast. (d) We show the modulation transfer functions for a perfect pinhole (diffraction limit, orange dots) and calculated by a Zemax simulation of the imaging system (blue line). The results of the measurement are shown by the green line. The contrast errors are smaller than the thickness of the green line. While these graphs were created with incoherent light, the purple line shows a measurement with coherent illumination. Interference effects at the central ring prevent the contrast from falling to zero. The black dashed line shows the cut-off frequency of the star target.

We also show a measurement of the MTF with coherent illumination (violet line in Fig. 2(d)). Because of the ability to form interference, the MTF of an ideal system is a step-function with contrast $C = 1$ for frequencies below $f_{\text{cut,diff}}/2$ and $C = 0$ for frequencies above it [25]. The contrast drops at smaller frequencies in our case because of the cut-off frequency of the star target $f_{\text{cut,star}}$. The absence of low spatial frequencies near the edge of the star target confirms that no clipping occurs in our setup. The contrast for spatial frequencies above $f_{\text{cut,star}}$ is significantly higher than in the incoherent case. We attribute this to two effects: First, the central ring of the star target forms diffraction rings. This causes the contrast to oscillate when the center of the star target is displaced from the center of the diffraction rings, which happens when the laser beam is not normal to the star target. Second, laser light features speckle noise, which is a pattern of random bright and dark spots. This speckle noise artificially boosts the contrast at frequencies above $f_{\text{cut,star}}$. However, we can correct for this in software by controlling the number of detected intensity peaks. For example, the R1L1S3P star target has 72 line pairs, and we set the contrast to zero if the number of bright peaks found in the image is outside the range of 62 to 82. The contrast above $f_{\text{cut,star}}$ then drops quickly to zero for both coherent and incoherent illumination.

Nonetheless we do not use this condition to gain information about the noise sources present in the setup and to show that incoherent illumination is less prone to alignment errors and speckle noise.

We conclude, that the theoretical resolution of the imaging system is computationally determined to be $f_{\mathrm{cut,diff}} = 250$ 1p/mm. Experimentally, we are limited by the test target and find a contrast $C = 0.420(3)$ at a spatial frequency of 100 lp/mm. The error is determined from the distribution of values of the intensity peaks.

4. Depth of field

The DOF is the axial distance the object can be moved and still be considered in focus. Because it is subjective and arbitrary what "still in focus" means, there are plenty of quantitative definitions of the DOF. We provide two DOF metrics – one yielding relatively large and the other relatively small values, so that most other definitions fall between these extremes. We exclude definitions that omit the camera's pixel size, either directly or indirectly, such as DOF = λ/NA^2, where λ is the wavelength and NA is numerical aperture. Intuitively, when the pixel size is comparable to the smallest resolvable spot of the image, changes in pixel size should affect the depth of field. The first, $\mathrm{DOF}_{\mathrm{C95}}$, is heuristically defined as the distance at which the image contrast decreases to 95 % of its maximum value at a spatial frequency of 20 lp/mm. The spatial frequency was chosen because it allows the determination of the contrast decrease for all aperture settings. The second, $\mathrm{DOF}_{\mathrm{geo}}$, is defined as the displacement from the ideal focus at distance f where the principal rays intersect a disk of a given size, such as the pixel size s_{pixel} (see Fig. 3(a)). Neglecting quadratic terms of s_{pixel}, $\mathrm{DOF}_{\mathrm{geo}}$ is expressed as:

$$\mathrm{DOF}_{\mathrm{geo}} \approx 4 \times s_{\mathrm{pixel}} f/d, \tag{2}$$

where f is the focal length and d the aperture of the imaging system. This definition corresponds to very little change in the MTF while the object moves through the $\mathrm{DOF}_{\mathrm{geo}}$. In Fig. 3(b) the $\mathrm{DOF}_{\mathrm{geo}}$ is calculated for different apertures assuming a pixel size $s_{\mathrm{pixel}} = 3.45$ µm. The DOF changes from 26 µm for a fully open aperture ($d = 22.4$ mm) to 203 µm for an aperture diameter of $d = 2.88$ mm.

Experimentally, we determine the DOF by measuring the through-focus MTF, while the TL is fixed to the minimal surface curvature setting. We use a motorized translation stage (LTS300/M from *Thorlabs*) to axially move the star target through the focal plane in ≈ 10 µm wide steps. After the translation stage halts, an image is taken and the MTF is determined. This is compared with the through-focus MTF shown in Fig. 3(c) to (e). The white central is a representation of $\mathrm{DOF}_{\mathrm{geo}}$. The white central region represents $\mathrm{DOF}_{\mathrm{geo}}$, within which the MTF varies by at most 0.3 %, approximately fulfilling the requirement of invariance across $\mathrm{DOF}_{\mathrm{geo}}$. Additionally, the contrast vanishes at lower spatial frequencies for small apertures, as expected from the resolution loss that accompanies increased DOF.

We experimentally determine the target position that allows the contrast to decrease to 95 % (blue lines in Fig. 3(c)-(e)) and plot the results in Fig. 3(b) (orange crosses). We find that the $\mathrm{DOF}_{\mathrm{C95}}$ changes from 0.12 mm to 1.1 mm. The $\mathrm{DOF}_{\mathrm{C95}}$ can be expressed in the same form as equation. 2, but with the right-hand side multiplied by 5.3 to account for the different definition of the width of the DOF. This shows the equivalence of the definition of the $\mathrm{DOF}_{\mathrm{geo}}$ and $\mathrm{DOF}_{\mathrm{C95}}$. We conclusively find that, regardless of the chosen DOF metric, the iris enables tunability of the DOF by approximately an order of magnitude. We note that for atomic clouds diffraction complicates image analysis and the identification of the optimal cloud position inside the DOF is challenging. However, density-density correlations of ultracold atoms, which effect the diffraction pattern, allows to bring clouds into focus with better accuracy than by identifying the peak optical density of cloud [27].

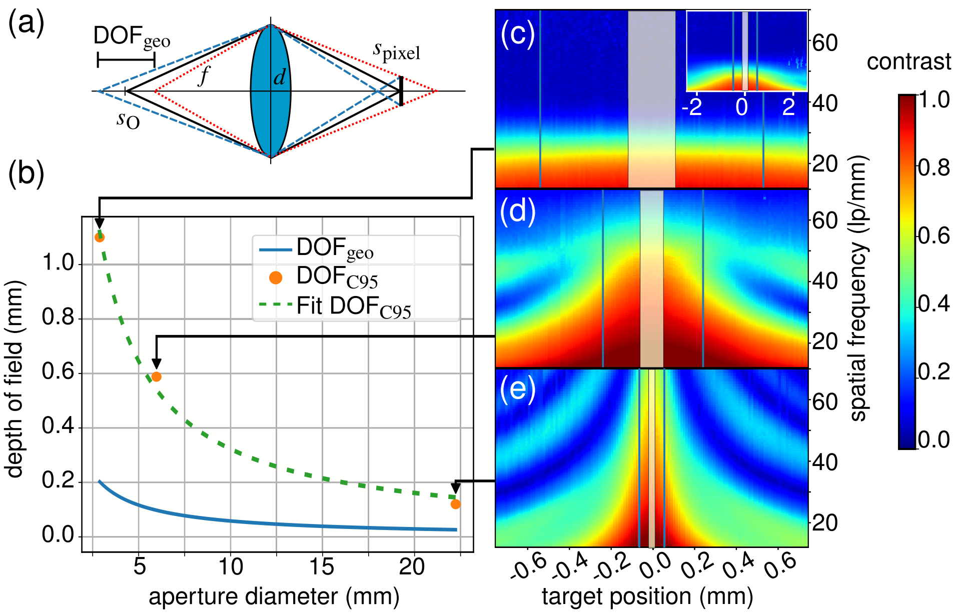

Fig. 3. Determination of the depth of field (DOF). (a) Schematic showing DOF$_{geo}$, which is determined by the focal length f, the pixel size s_{pixel} and the lens diameter d. (b) shows the calculated DOF$_{geo}$ (blue line) vs. aperture diameter. We determined experimentally the DOF$_{C95}$ (orange crosses, see text for explanation) and fit the data (green dotted line) with a function in the form of Eq. (2), but with an additional scaling parameter. On the right, we show through-focus scans for the minimal aperture (c), an intermediate aperture (d) and fully open iris (e). The highlighted area shows the DOF according to Eq. (2), the blue vertical lines mark the DOF$_{C95}$. In (c) the DOF is too large to see the contrast significantly dropping over the scan range. The inset shows a larger scan range.

Finally, we observe a fringe pattern in the through-focus MTF plots, most clearly in Fig. 3(e). This spurious resolution arises from spatial chirp in defocused images [28]. In the star-target images, it also manifests as a phase reversal of the stripe pattern, although the MTF itself is insensitive to optical phases [25].

5. Distortion

Distortion is a form of optical aberration, where straight lines appear curved in the image. Since this aberration alters the apparent distance between two points, distortion leads to systematic uncertainties in determining the position and hence, e.g. the estimation of the velocities of the atomic clouds. Experimentally, we determine the distortion by imaging a grid target (R1L3S3P from *Thorlabs*, 500 µm spacing), which we place in the focal plane of the imaging system (see Fig. 4(a)). The grid points (x, y) will be used to assess the amount of distortion.

Distortion is commonly described by the Brown–Conrady model [29,30], with parameters obtainable from open-source tools such as OpenCV [31]. These libraries output coefficients that are dependent on the specific implementation and are directly comparable across libraries. We state the distortion coefficients of the Brown-Conrady model determined by OpenCV in the Supplement 1 [32]. To quantify distortion in physically meaningful units for atomic physics, we additionally created a more suitable projection-error method.

We create an ideal grid from the central region of the image where the amount of distortion is expected to be small. In our case, we use 5×4 grid points in the center to form the ideal grid.

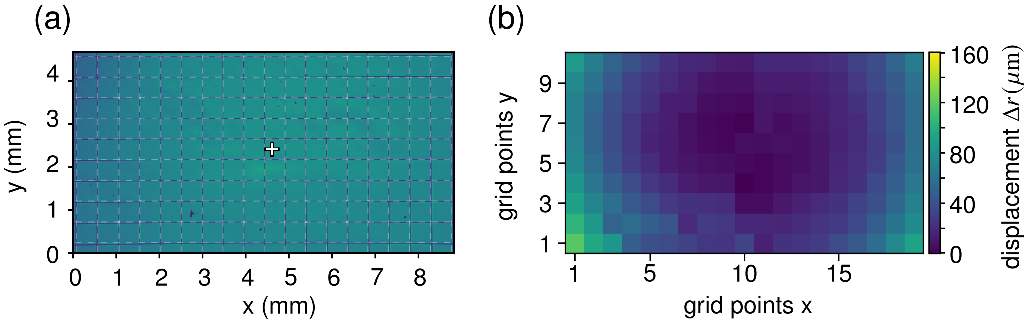

Fig. 4. Determination of the optical distortion. (a) Image of a grid target with 500 μm spacing, which is used this to determine the distortion. The cross shows the optical axis and white lines are a guide to the eye. Pincushion distortion is present, but only visible near the edges of the image. (b) The distance Δr of the measured grid points and an ideal grid is shown for a TL setting of $\Delta f_{\mathrm{TL}} = 0$ mm. To create the ideal grid, we take 5×4 grid points from the center of the image, where the amount of distortion is expected to be negligible. From the mean grid spacing we generate the ideal grid and overlay it with the center grid. We find pincushion distortion, which causes a maximum displacement of the grid points of 160 μm at the very edges of the image.

Compared to the ideal grid, the measured grid points will be shifted in x- and y-direction in the image plane, which can be described by a translation in Δx and Δy direction, or by the Euclidean distance $\Delta r = \sqrt{\Delta x^2 + \Delta y^2}$.

Figure 4(a) shows an image of a grid target taken with our imaging system without tuning of the EFL. The analysis reveals an increasing magnification with increasing distance to the optical axis, known as pincushion distortion. In Fig. 4(b) we show the displacement r. It increases towards the edge of the image, which is a typical signature of radial distortion. We find a maximum displacement Δr in our setup of 160 μm. A similar imaging system, but without the TL reveals a maximum displacement r below 10 μm. The TL therefore introduces most of the optical distortion. This is expected since the surface of the liquid lens is not optimized to reduce aberrations. Even though distortion is increased by more than an order of magnitude compared to a conventional imaging system, the effect on atom optic experiments can be mitigated. With the method shown here, it is possible to map the distortion. Since this method obtains corner points in a similar fashion as conventional implementations for distortion correction [31], post-correcting the images to reduce position errors for the atomic clouds is straight forward (see [32], figure S1).

6. Tunability of the front focal length

In this section we investigate the quality of the imaging for different s_{O} in a range of 88.9 mm ± 5 mm. We identify the focus by measuring the through-focus MTF as described in section 4. In the through-focus MTF plots, we select a suitable spatial frequency (here 60 lp/mm) and determine the position of the test target that gives the maximum contrast.

Example plots for the through-focus MTF are shown in Fig. 5(a). As the TL setting changes from the central $\Delta f_{\mathrm{TL}} = 0$ position, the DOF increases by a factor of 1.5 and the through-focus MTF becomes asymmetric around the focus. This effect is associated with the presence of optical aberrations [33], which increase with the curvature of the TL surface and reduces optical resolution. For example, at 100 lp/mm the optimal contrast $C = 0.420(3)$ drops to about $C \approx 0.3$ for a ±5 mm shift in object distance. Nevertheless, this remains sufficient to resolve atomic clouds, which typically span a few tens of micrometers [1]. Adjusting the TL also changes the magnification, as the ratio of the front to the rear focal length changes (see section 2). The magnification was experimentally determined as described in section 3. The magnification changes according to $m(\Delta f_{\mathrm{TL}}) = f_{\mathrm{back}}/(f_{\mathrm{front}} + \Delta f_{\mathrm{TL}})$. However, we simplify our evaluation to a linear function $m(\Delta f_{\mathrm{TL}})$, as the change Δf_{TL} is small compared to the EFL (see Fig. 5(b)). The green line, which represents a linear regression to the data points, describes the measurement data sufficiently well, as 80 % of the data points lie within a standard error (green area).

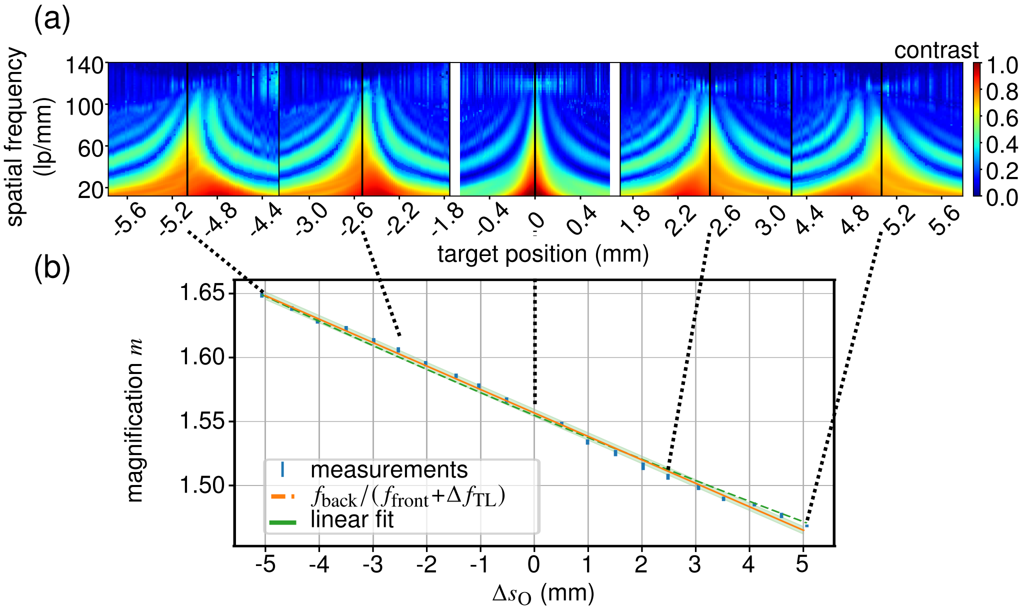

Fig. 5. Tunability of the imaging system. We change the EFL to tune the object distance s_{O} by $\Delta s_{\mathrm{O}} = \pm 5$ mm relative to the center of 88.9 mm. (a) Five exemplary scans of the star target through the focal plane using the translation stage. In each scan, the black line marks the focal length, where the contrast at 60 lp/mm is maximum. (b) The magnification for different TL settings. Magnification values are averages over 11 images, with mean errors shown. The magnification m changes according to $f_{\mathrm{back}}/(f_{\mathrm{front}} + \Delta f)$ (orange dashed line). Since the change in focal length is small compared to the total focal length, a linear dependence (green solid line) describes the data well within standard deviation (green area).

The method of determining s_{O} by capturing the through-focus MTF also allows for sensitive characterization measurements of our imaging system. For example, we determine the smallest increment $\Delta s_{\mathrm{O,min}}$ of the object distance. As mentioned in section 2, the TL is motorized by a Piezo-driven rotary stepper motor. Stepper motors work on the principle of stick and slip and therefore feature a minimal step size. By performing up to 10 steps with the motor, we are able to determine the incremental step size to $\Delta s_{\mathrm{O,min}} = 2.0 \pm 0.1$ µm. We conclude that this step size is small enough to smoothly scan s_{O} since this step size is much smaller than the measured DOF for all settings of the tunable iris aperture (see section 4).

Finally we investigate the dependence of the object distance s_{O} on temperature. We put the imaging system in a thermal chamber, evenly increase the temperature to 45 ◦C and allow the system to reach thermal equilibrium. The temperature is measured at several points within the chamber and directly on the housing of the TL using negative temperature coefficient thermistors attached with tape. We then open one side of the chamber and allow the system to cool down to room temperature. As the imaging system cools down by 10 K for over half an hour, we continuously perform through-focus scans to determine s_{O}. We find a thermal coefficient τ, which describes the change of s_{O} with temperature, of $\tau = -370 \pm 50$ µm K^{-1}. The minus sign indicates that the focal length is shifted towards the imaging system. The thermal coefficient τ shows, that a temperature change of 1 K is enough to escape the original DOF. During operation in a thermally controlled laboratory, we observed no measurable temperature-induced drift of the focal length. Thus, the apparatus in which the imaging system is deployed must provide a stable thermal environment and include temperature monitoring near the optics. If such stability cannot be guaranteed, active temperature regulation, e.g., using Peltier elements, can be implemented. Additionally, we believe that the strong temperature dependence of the imaging system is related to the large aperture of the liquid lens. We found that a TL with a smaller aperture, 16 mm instead of 20 mm, leads to a thermal coefficient τ an order of magnitude smaller. We attribute this behavior to the reduced liquid volume inside the lens.

7. Conclusion

The ever growing complexity of experiments and the increasing number of applications of cold atoms present a significant challenge to conventional imaging systems using a fixed focal length and depth of field. Defocus-based imaging techniques [6], atom clouds transported along the line of sight [8], arrays of cold atoms used in inertial sensing [17] and quantum bubbles [18,20] require imaging capabilities beyond fixed-focus systems. To address these challenges, we have developed and tested an imaging system with variable focus and tunable depth of field for absorption detection of ultracold atoms. While tunable lenses and adjustable irises are well-established optical components, their capabilities for controlling object distance and depth of field in cold atom absorption imaging have not yet been fully exploited.

The optical resolution of the imaging system was evaluated using the MTF, with a measured contrast of $C = 0.420(3)$ at 100 lp/mm, comparable to other conventional detection systems [7,12]. By closing the iris aperture, the depth of field can be increased from a few tens to several hundred micrometers, enabling a trade-off between high-resolution imaging with a shallow focus and capturing objects distributed over varying axial positions with an extended focus range.

By performing focus scans, we demonstrated tunability of the object distance around 88.9 mm over a range of ±5 mm, with step sizes of 2.0(1) μm. This flexibility comes at the cost of image distortion introduced by the liquid lens. We quantified this distortion by comparing recorded images with an ideal reference grid – a method particularly suitable for atomic physics, as it provides the rectilinear projection error directly in units of length. Using standard correction techniques [31], these distortions can be effectively compensated. Finally, we observed a thermal dependence of the focal length of −370(50) μm Kˆ{−1} near 25 ◦C, which poses requirements on thermal management in the experimental apparatus, but not on the imaging system itself.

The compact and robust design renders the system appropriate for operation in harsh or remote environments, including mobile quantum sensors [34] and space-based platforms such as the International Space Station [21,35].

Funding. Deutsche Forschungsgemeinschaft (EXC-2123 QuantumFrontiers- 390837967).

Acknowledgment. We thank Maximilian Schier for his guidance with the OpenCV library. This work is partially funded by the Deutsche Forschungsgemeinschaft (DFG, German Research Foundation) under Germany's Excellence Strategy – EXC-2123 QuantumFrontiers – 390837967.

Disclosures. The authors declare no conflicts of interest.

Data availability. Data underlying the results presented in this paper are not publicly available at this time but may be obtained from the authors upon reasonable request.

Supplemental document. See Supplement 1 for supporting content.

References

1. W. Ketterle, D. S. Durfee, and D. M. Stamper-Kurn, "Making, probing and understanding bose-einstein condensates," (1999).
2. G. Reinaudi, T. Lahaye, Z. Wang, *et al.*, "Strong saturation absorption imaging of dense clouds of ultracold atoms," Opt. Lett. **32**(21), 3143 (2007).

3. M. Pappa, P. C. Condylis, G. O. Konstantinidis, *et al.*, "Ultra-sensitive atom imaging for matter-wave optics," New J. Phys. **13**(11), 115012 (2011).
4. A. Reinhard, J.-F. Riou, L. A. Zundel, *et al.*, "Dark-ground imaging of high optical thickness atom clouds," Opt. Commun. **324**, 30–33 (2014).
5. C. Deppner, W. Herr, M. Cornelius, *et al.*, "Collective-mode enhanced matter-wave optics," Phys. Rev. Lett. **127**(10), 100401 (2021).
6. A. R. Perry, S. Sugawa, F. Salces-Carcoba, *et al.*, "Multiple-camera defocus imaging of ultracold atomic gases," Opt. Express **29**(11), 17029–17041 (2021).
7. D. A. Smith, S. Aigner, S. Hofferberth, *et al.*, "Absorption imaging of ultracold atoms on atom chips," Opt. Express **19**(9), 8471–8485 (2011).
8. J. Léonard, M. Lee, A. Morales, *et al.*, "Optical transport and manipulation of an ultracold atomic cloud using focus-tunable lenses," New J. Phys. **16**(9), 093028 (2014).
9. S.-H. Jo and S.-C. Park, "Design and analysis of an 8x four-group zoom system using focus tunable lenses," Opt. Express **26**(10), 13370–13382 (2018).
10. X. Hu, G. Wang, Y. Zhang, *et al.*, "Large depth-of-field 3d shape measurement using an electrically tunable lens," Opt. Express **27**(21), 29697–29709 (2019).
11. D. Barredo, V. Lienhard, S. de Léséleuc, *et al.*, "Synthetic three-dimensional atomic structures assembled atom by atom," Nature **561**(7721), 79–82 (2018).
12. J. Rudolph, W. Herr, C. Grzeschik, *et al.*, "A high-flux BEC source for mobile atom interferometers," New J. Phys. **17**(6), 065001 (2015).
13. X. Wu, Z. Pagel, B. S. Malek, *et al.*, "Gravity surveys using a mobile atom interferometer," Sci. Adv. **5**(9), eaax0800 (2019).
14. G. Unnikrishnan, C. Beulenkamp, D. Zhang, *et al.*, "Long distance optical transport of ultracold atoms: A compact setup using a Moiré lens," Rev. Sci. Instrum. **92**(6), 063205 (2021).
15. H. Swan, A. Torchylo, M. J. V. de Graaff, *et al.*, "High-fidelity holographic beam shaping with optimal transport and phase diversity," Opt. Express **33**(3), 6290–6303 (2025).
16. A. R. Bayanna, R. E. Louis, S. Chatterjee, *et al.*, "Membrane-based deformable mirror: intrinsic aberrations and alignment issues," Appl. Opt. **54**(7), 1727–1736 (2015).
17. K. Stolzenberg, C. Struckmann, S. Bode, *et al.*, "Multi-axis inertial sensing with 2d matter-wave arrays," Phys. Rev. Lett. **134**(14), 143601 (2025).
18. K. Sun, K. Padavić, F. Yang, *et al.*, "Static and dynamic properties of shell-shaped condensates," Phys. Rev. A **98**(1), 013609 (2018).
19. N. Lundblad, R. A. Carollo, C. Lannert, *et al.*, "Shell potentials for microgravity Bose-Einstein condensates," Nature Partner Journals Microgravity **5**, 30 (2019).
20. R. A. Carollo, D. C. Aveline, B. Rhyno, *et al.*, "Observation of ultracold atomic bubbles in orbital microgravity," Nature **606**(7913), 281–286 (2022).
21. K. Frye, S. Abend, W. Bartosch, *et al.*, "The Bose-Einstein condensate and cold atom laboratory," EPJ Quantum Technol. **8**(1), 1 (2021).
22. R. Stephens, "Probabilistic approach to the hough transform," Image and Vision Computing **9**(1), 66–71 (1991).
23. R. Fischer and B. Tadic, *Optical System Design* (McGraw-Hill's access Engineering, 2000).
24. D. A. Rowlands, *Physics of Digital Photography (Second Edition)* 2053–2563 (2020).
25. J. W. Goodman, *Introduction to Fourier optics* (Englewood, Colo, 2005), 3rd ed.
26. I. Estévez, J. C. Escalera, Q. P. Stefano, *et al.*, "Image enhancement by spatial frequency post-processing of images obtained with pupil filters," Opt. Commun. **380**, 21–27 (2016).
27. A. Putra, D. L. Campbell, R. M. Price, *et al.*, "Optimally focused cold atom systems obtained using density-density correlations," Rev. Sci. Instrum. **85**(1), 013110 (2014).
28. H. Strasburger, M. Bach, and S. P. Heinrich, "Blur unblurred—a mini tutorial," i-Perception **9**(2), 2041669518765850 (2018).
29. D. Brown, "Decentering distortion of lenses," Photogrammetric Engineering **32**, 444–462 (1996).
30. A. E. Conrady, "Decentred Lens-Systems," Mon. Not. R. Astron. Soc. **79**(5), 384–390 (1919).
31. OpenCV Documentation, "Camera calibration and 3D reconstruction," https://docs.opencv.org/4.x/d9/d0c/group__calib3d.html (2022). Accessed: (2024-07-31).
32. K. Frye-Arndt, A. Wacker, P. Brunssen, *et al.*, "A focus and depth of field tunable detection system for compact quantum sensors supplemental document," Figshare.
33. R. C. Bakaraju, K. Ehrmann, E. B. Papas, *et al.*, "Depth-of-focus and its association with the spherical aberration sign. a ray-tracing analysis," Journal of Optometry **3**(1), 51–59 (2010).
34. A. Acín, I. Bloch, H. Buhrman, *et al.*, "The quantum technologies roadmap: a European community view," New J. Phys. **20**(8), 080201 (2018).
35. D. C. Aveline, J. R. Williams, E. R. Elliott, *et al.*, "Observation of Bose–Einstein condensates in an Earth-orbiting research lab," Nature **582**(7811), 193–197 (2020).